ACS OMEGA

http://pubs.acs.org/journal/acsodf

Article

Bio-Conjugated Magnetic-Fluorescence Nanoarchitectures for the Capture and Identification of Lung-Tumor-Derived Programmed Cell Death Lighand 1-Positive Exosomes

Avijit Pramanik, Shamily Patibandla, Ye Gao, Lauren R. Corby, Md Mhahabubur Rhaman, Sudarson Sekhar Sinha, and Paresh Chandra Ray*

Cite This: *ACS Omega* 2022, 7, 16035−16042

Read Online

ACCESS | Metrics & More | Article Recommendations | Supporting Information

ABSTRACT: As per the American Cancer Society, lung cancer is the leading cause of cancer-related death worldwide. Since the accumulation of exosomal programmed cell death ligand 1 (PD-L1) is associated with therapeutic resistance in programmed cell death 1 (PD-1) and PD-L1 immunotherapy, tracking PD-L1-positive (PD-L1 (+)) exosomes is very important for predicting anti-PD-1 and anti-PD-L1 therapy for lung cancer. Herein, we report the design of an anti-PD-L1 monoclonal antibody-conjugated magnetic-nanoparticle-attached yellow fluorescent carbon dot (YFCD) based magnetic-fluorescence nanoarchitecture for the selective separation and accurate identification of PD-L1-expressing exosomes. In this work, photostable YFCDs with a good photoluminescence quantum yield (23%) were synthesized by hydrothermal treatment. In addition, nanoarchitectures with superparamagnetic (28.6 emu/g), biocompatible, and selective bioimaging capabilities were developed by chemically conjugating the anti-PD-L1 antibody and YFCDs with iron oxide nanoparticles. Importantly, using human non-small-cell lung cancer H460 cells lines, which express a high amount of PD-L1 (+) exosomes, A549 lung cancer cells lines, which express a low amount of PD-L1 (+) exosomes, and the normal skin HaCaT cell line, which does not express any PD-L1 (+) exosomes, we demonstrate that nanoarchitectures are capable of effectively separating and tracking PD-L1-positive exosomes simultaneously. Furthermore, as a proof-of-concept of clinical setting applications, a whole blood sample infected with PD-L1 (+) exosomes was analyzed, and our finding shows that this nanoarchitecture holds great promise for clinical applications.

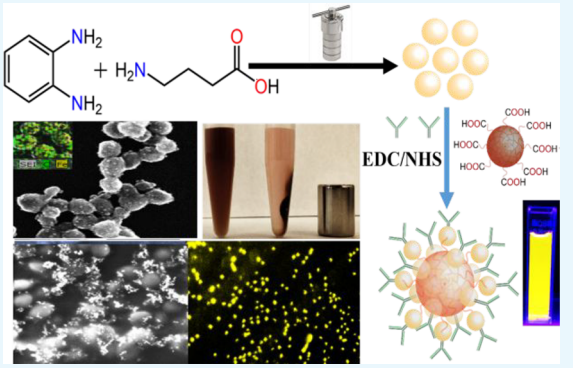

1. INTRODUCTION

As per the World Health Organization (WHO) and the American Cancer Society, even in 2021, lung cancer remains the leading cause of cancer-related death.[1,2] Among lung cancer patients, non-small-cell lung cancer (NSCLC) causes most of the deaths.[3−7] The reported lower survival rate for NSCLC is mainly due to its diagnosis at the advanced stages.[3−7] Recent advancement shows that immunotherapies using antibodies that target the programmed cell death 1 (PD-1) and programmed cell death ligand 1 (PD-L1) pathways (PD-1/PD-L1) have enhanced antitumor effects for NSCLC patients, which help to increase the survival rate.[8−13] In the last five years, clinical data have shown that anti-PD1/PDL1 therapy produced a limited response for many lung cancer patients.[10−16]

Recent clinical studies show that the excessive accumulation of exosomal PDL1 in the lymph node is associated with therapeutic resistance in PD-1/PD-L1 immunotherapy.[8−16] Due to the above fact, evaluating the presence of exosomal PD-L1 is very important to determine the immune escape and tumor progression.[12−17]

Herein, we report the design of an anti-PDL1 monoclonal antibody-conjugated magnetic-nanoparticle-attached yellow fluorescence carbon dot (YFCDs) based magnetic-fluorescence nanoarchitecture, as shown in Figure 1, which is capable of the targeted separation and accurate identification of PD-L1-expressing exosomes.

Exosomes are smaller sized (>200 nm) membrane vesicles that contain biologically active m-RNA, proteins, lipids, DNA, and other nucleic acids.[12−22] It is now well-documented that exosomes play a major role in the regulation of metastasis via cell-to-cell communication.[12−22] Several clinical studies indicate that exosome-carrying PD-L1 can be associated with a suppression of the antitumor immune response for

Received: February 28, 2022
Accepted: March 31, 2022
Published: April 25, 2022

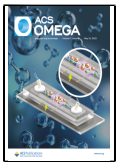

https://doi.org/10.1021/acsomega.2c01210
ACS Omega 2022, 7, 16035−16042

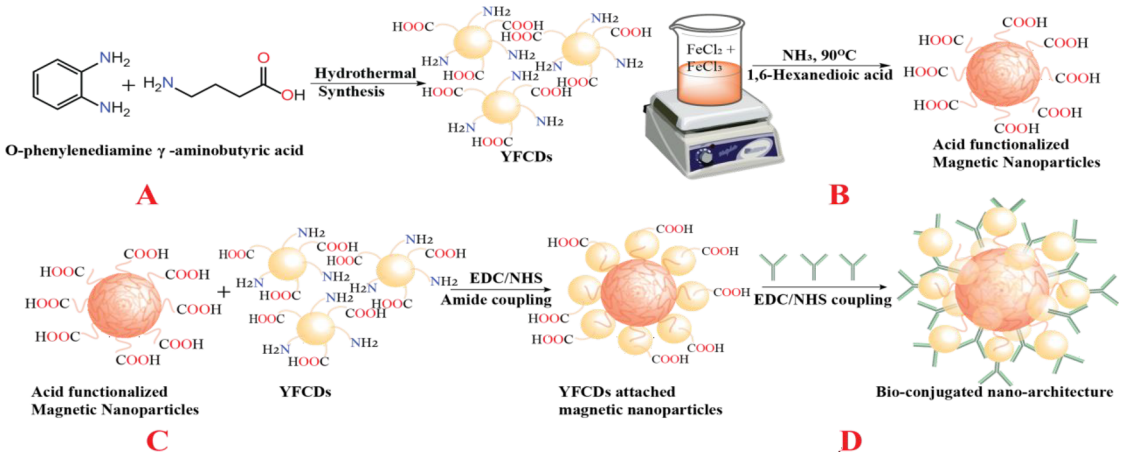

Figure 1. Scheme showing the design of the anti-PD-L1 monoclonal antibody-conjugated magnetic-fluorescence nanoarchitecture. (A) Hydrothermal synthesis of YFCDs from *o*-phenylenediamine and 4-aminobutyric acid. (B) Synthesis of acid-functionalized magnetic nanoparticles. (C) Synthesis of YFCD-attached magnetic nanoparticles. D) Synthesis of the anti-PD-L1 monoclonal antibody-attached nanoarchitecture.

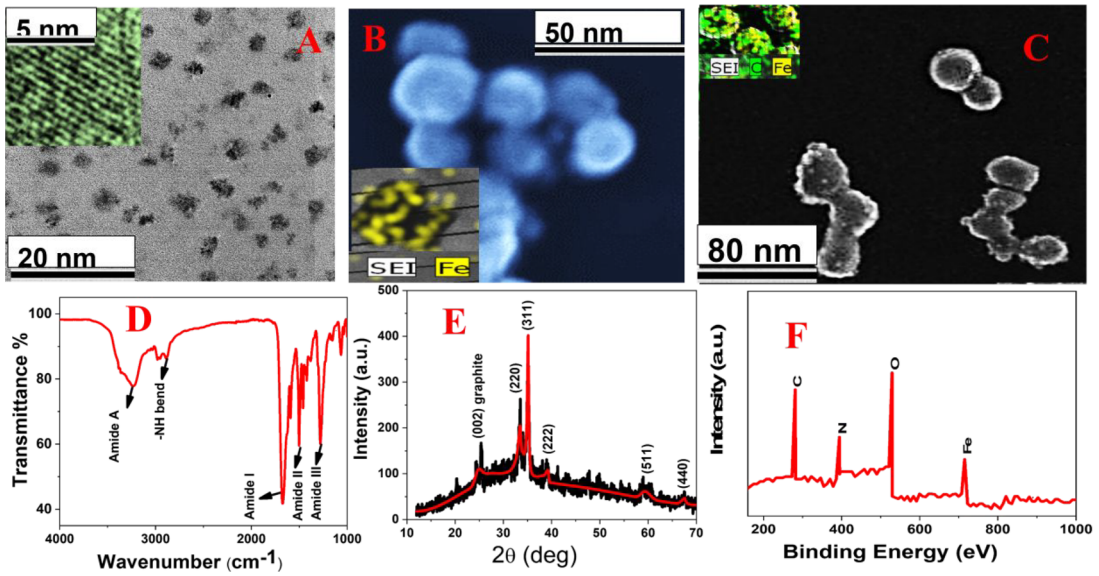

Figure 2. (A) TEM image showing the morphology of yellow luminescent carbon dots derived from *o*-phenylenediamine and 4-aminobutyric acid. The inserted HR-TEM image shows graphite-type lattice fringes with an interplanar spacing of 0.35 nm for carbon dots derived from *o*-phenylenediamine and 4-aminobutyric acid. (B) TEM image showing the morphology of the acid-functionalized magnetic nanoparticles. The inserted EDX elemental map shows the presence of Fe. (C) TEM image showing the morphology of the yellow luminescent carbon dot-attached magnetic nanoparticle. The inserted EDX elemental map shows the presence of Fe and C. (D) FTIR spectrum from the yellow luminescent carbon dot-attached magnetic nanoparticle showing the presence of amide A, amide-I, amide-II, amide-III, and other bands. (E) The X-ray diffraction pattern from the yellow luminescent carbon dot-attached magnetic nanoparticle confirms the presence of (002) indices for graphitic carbon and (220), (311), (222), (511), and (440) indices for the magnetic nanoparticles. (F) The XPS spectrum from the yellow luminescent carbon dot-attached magnetic nanoparticle confirms peaks at 284.8, 398.1, 532.5, and 711.2 eV due to Fe, O, N and C, respectively.

NSCLC.[10−17] As a result, analyzing the PD-L1 expression exosomes in the tumor microenvironment is very important for the clinical success of lung cancer treatment.[12−17] Since biological fluids containing exosomes also have cell debris, proteins, different types of other vesicles, and several biologically important molecules, as we and others have reported before, isolation and enrichment steps are the initial steps to separate an exosome before it can be analyzed.[12−22] For this purpose, we have designed an immunomagnetic nanoarchitecture that can be used to isolate the PD-L1-positive (PD-L1 (+)) exosome from the cell culture and a whole-blood sample. In our design, an anti-PD-L1 antibody is used to bind the PD-L1 (+) exosome, and the exosome-attached magnetic nanoparticles are separated using a simple bar magnet. In addition, we have used YFCDs for the accurate identification of the PD-L1 (+) exosome after magnetic separation. Due to their simple large-scale synthesis, low toxicity, high fluorescence quantum yield, and excellent chemical stability,[23−37] YFCDs were used for the bioimaging of the PD-L1 (+) exosome. We used yellow fluorescence for exosome imaging because it has better tissue penetration and to avoid blue autofluorescence from the cell matrix.[30−34]

2. RESULTS AND DISCUSSION

2.1. Synthesis, Microscopy Characterization, and Optical Properties of Yellow Fluorescence Carbon Dots. The yellow fluorescent carbon dots (YFCDs) were

https://doi.org/10.1021/acsomega.2c01210
ACS Omega 2022, 7, 16035−16042

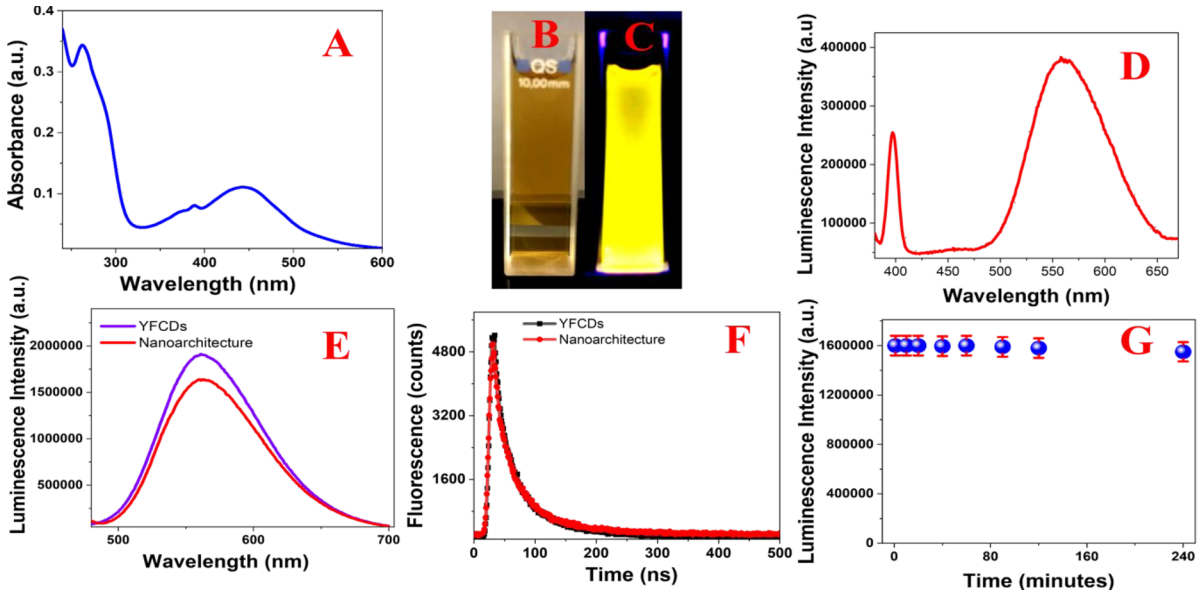

Figure 3. (A) Absorption spectrum of the YFCDs, which indicates two absorption peaks. The $\pi-\pi^*$ transition is visible at 260 nm, and the other transition due the functional groups conjugated on CDs is visible at 436 nm. (B) Photograph of YFCDs in the absence of UV light. (C) Photograph of YFCDs in the presence of UV light showing the strong yellow emission. (D) Emission spectrum of YFCDs in the presence of 300 nm excitation light. (E) Emission spectra of YFCDs and the anti-PD-L1 monoclonal antibody-conjugated magnetic-nanoparticle-attached YFCD-based nanoarchitecture in the presence of 480 nm excitation light. (F) Plot showing the time-resolved photo luminescence decay of YFCDs and the anti-PD-L1 monoclonal antibody-conjugated magnetic-nanoparticle-attached YFCD-based nanoarchitecture in the presence of 480 nm excitation light. (G) Luminescence intensity of the anti-PD-L1 monoclonal antibody-conjugated magnetic-nanoparticle-attached YFCDs as a function of time in the presence of 480 nm excitation light. The experiment was performed five times, and error bars were calculated from the standard deviation.

synthesized by a hydrothermal treatment using *o*-phenylenediamine and γ-aminobutyric acid.[30] The experimental details are reported in the Supporting Information. For this purpose, *o*-phenylenediamine and γ-aminobutyric acid were added to distilled water, and the mixture was sonicated for 30 min. After that, the solution was heated for 8 h at 160 °C using a Teflon-lined stainless-steel autoclave. Next, we cooled the mixture to room temperature and then filtered it through membrane filter paper with a pore size of 0.45 μm. After that, we dialyzed the mixture with 3.5 KD MWCO Snakeskin dialysis tubing for three days. Finally, the pure solid product was obtained after lyophilization for 3−5 days by a freeze-drying process.

To characterize the YFCDs, we used high-resolution tunneling electron microscopy (HR-TEM), X-ray photoelectron spectroscopy (XPS), absorption spectroscopy, and fluorescence spectroscopy in addition to photoluminescence quantum yield (PLQY), fluorescence lifetime analysis, and dynamic light scattering (DLS) measurements[20,31,32,34] as reported in Figure 2 and Table S1 in the Supporting Information. The TEM image reported in Figure 2A shows the morphology of the YFCDs and indicates that the size of the YFCDs is ∼5 ± 2 nm. The size measurement by TEM matches very well with the DLS data, as reported in Table S1 in the Supporting Information. The inserted high-resolution TEM image indicates graphite type lattice fringes, where the interplanar spacing is ∼0.35 nm. From the energy-dispersive X-ray spectroscopy (EDX) analysis, we determined amount of C, N, O, and H to be ∼60%, ∼18%, ∼12%, and ∼10%, respectively. Figure 2F shows the XPS data for the YFCDs, which clearly indicate the presence of a C 1s peak at 284.8 eV, an O 1s peak at 532.5 eV, and a N 1s peak at 398.1 eV.[30−33] On the basis of the XPS and EDX data, we can conclude that YFCDs contains both carboxy and amine groups in the surface, as shown in Figure 1A.

Figure 3A shows the absorption spectra of the YFCDAs, which clearly show two absorption peaks. The first higher-energy absorption peak, which is mainly due to the $\pi-\pi^*$ transition of C−C bonds within the cores of the YFCDs, was observed at 260 nm.[30−32] On the other hand, the second lower-energy absorption peak, which is mainly due to the n → π^* transitions in C−O bonds originating from the surface functional groups attached to the carbon backbone of YFCDs, was observed at 436 nm.[30−33] Panels B and C in Figure 3 show photographs of the YFCDs in the presence and absence of 380 nm UV light, respectively. The photograph shown in Figure 3C clearly shows the emission of strong yellow fluorescence from the YFCDs in the presence of 380 nm UV light. Panels D and E of Figure 3 show the emission spectra of the YFCDs at excitation wavelengths of 300 and 480 nm, respectively. We observed two emission peaks when the YFCDs were excited at 300 nm, as shown in Figure 3D. The first sharp peak is visible around λ_{max} = 390 nm of the emission, which is mainly due to the core emission from YFCDs. The sharp emission arises due to quantum confinement effects and the presence of π-domains within the cores of the YFCDs. The second broad peak is visible around λ_{max} = 570 nm of the emission, which is mainly due to the surface −OH, −NH, —C═O functional groups and other groups bonded to the cores of the YFCDs.[30−33] We observed only one emission peak when the YFCDs were excited at 480 nm, as shown in Figure 3E. The observed broad peak is around 570 nm, showing that the broad luminescence spectrum remains unchanged for YFCDs even when the the excitation wavelength is varied from 300 to 480 nm. To measure the photoluminescence quantum yield (PLQY), we used quinine sulfate as a standard (QY = 54%).[20,31−33] By measuring the fluorescence intensity from a standard and the YFCDs, we determined the PLQY for YFCDS is 0.31 at an excitation wavelength of 480 nm. Figure 3F shows the time-

https://doi.org/10.1021/acsomega.2c01210
ACS Omega 2022, 7, 16035−16042

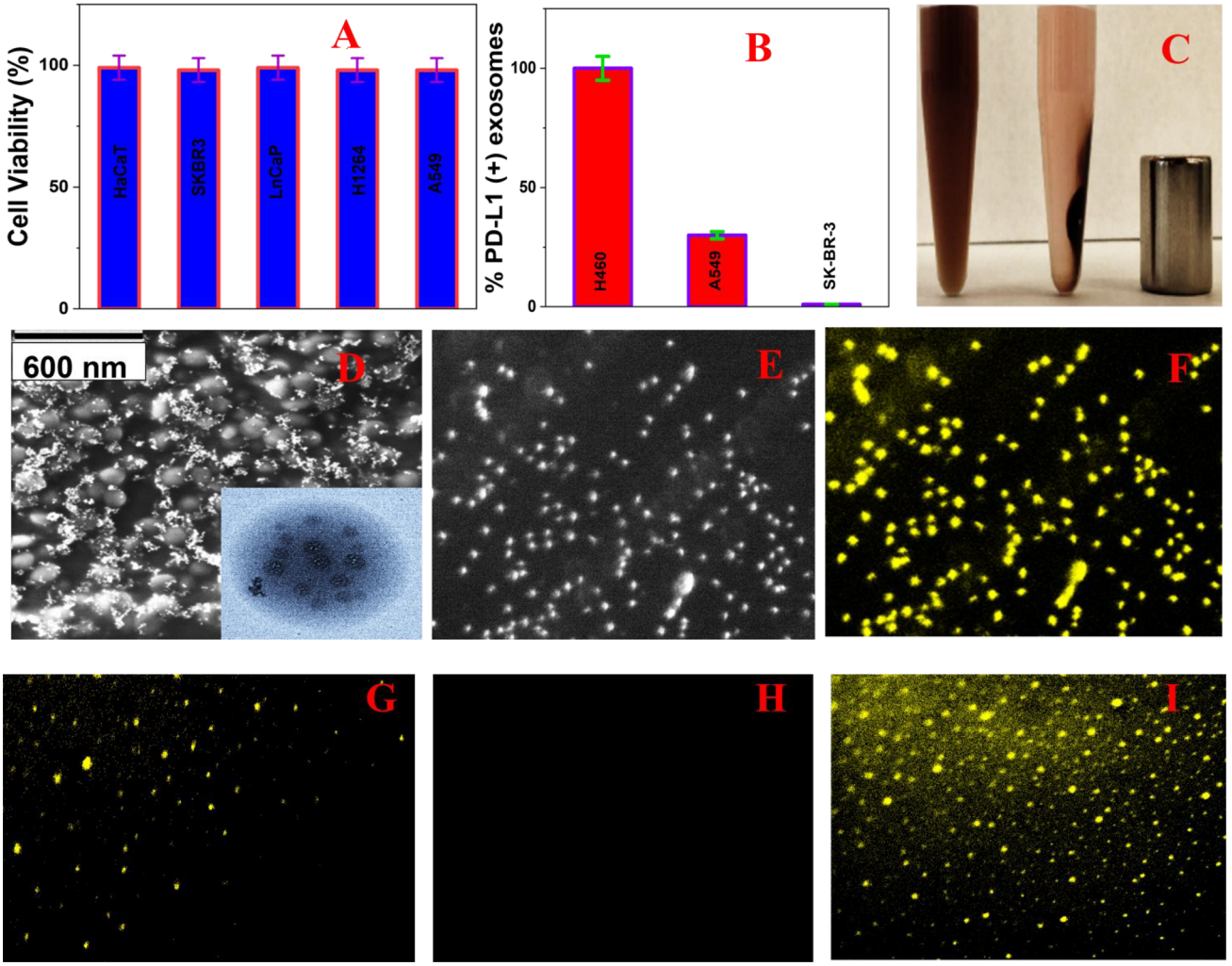

Figure 4. (A) Viability of LaCaT normal skin cells, SK-BR-3 breast cancer cells, LnCaP prostate cancer cells, and H1264 and A549 lung cancer cells after 24 h of treatment with the nanoarchitecture. The experiment was performed five times, and error bars were calculated from the standard deviation. (B) The percent of PD-L1-positive exosomes separated from different cell lines. We used the human PD-L1 ELISA kit for the quantitation of the PD-L1 (+) exosomes. (C) Photograph showing the separation of the PD-L1 (+) exosome-attached nanoarchitectures using bar magnet. The experiment was performed five times, and error bars were calculated from the standard deviation. (D) SEM image of PD-L1 (+) exosomes after magnetic separation from the H460 cell line. The inserted TEM image and SEM image show the nanostructures attached the PD-L1 (+) exosomes. (E) Bright-field image of the PD-L1 (+) exosome-attached nanoarchitectures after magnetic separation from the H460 cell line. (F) Fluorescence image showing the high number of PD-L1 (+) exosome-attached nanoarchitectures after magnetic separation from the H460 cell line. (G) Fluorescence image showing the low number of PD-L1 (+) exosomes after magnetic separation from the A549 cell line using the nanoarchitecture. (H) Fluorescence image showing the absence of PD-L1 (+) exosomes after magnetic separation from the HaCaT cell line using the nanoarchitecture. (I) Fluorescence image showing PD-L1 (+) exosome-attached nanoarchitectures after magnetic separation from the whole-blood sample.

dependent photoluminescence decay profiles for YFCDs at an excitation wavelength of 480 nm. The observed that the time-resolved decays can be fit very well by a double -exponential function with τ_1 = 1.8 ns and τ_3 = 11.4 ns.

2.2. Synthesis, Microscopy Characterization, Magnetic and Optical Properties of the Anti-PD-L1 Monoclonal Antibody-Conjugated Nanoarchitecture. We have designed an anti-PD-L1 monoclonal antibody-conjugated magnetic-nanoparticle-attached YFCD-based multifunctional magnetic-fluorescence nanoarchitecture using a four-step procedure, as reported in Figure 1. In the first step, the yellow fluorescent carbon dots were synthesized as discussed in the previous section. In second step, carboxylic acid-functionalized magnetic nanoparticles were synthesized. As shown in Figure 1B, we used a coprecipitation method with ferric chloride and 1,6-hexanedioic acid for this purpose.[31−33] The experimental details are reported in the Supporting Information. After the reaction between ferric chloride and 1,6-hexanedioic acid was complete, the black precipitate was separated using a neodymium magnet.[31,32] The TEM image shown in Figure 2B shows the morphology of the acid-functionalized magnetic nanoparticle and indicates that the nanoparticle's size is ∼20 ± 5 nm. The size measurement by TEM matches very well with the DLS data, as reported in Table S1 in the Supporting Information. Inserted energy-dispersive X-ray spectroscopy (EDX) mapping data from the magnetic nanoparticles, as reported in Figure 2B, indicates the presence of Fe. We measured the superparamagnetic properties using as SQUID magnetometer, as we have reported

https://doi.org/10.1021/acsomega.2c01210
ACS Omega 2022, 7, 16035−16042

before,[31−33] and obtained a specific saturation magnetization of ∼34.6 emu/g.

As shown in the Figure 1C, in the third step we developed the multifunctional magnetic fluorescence nanoplatform by conjugating the acid-functionalized magnetic nanoparticle with the amine group of the YFCDS. The experimental details are reported in the Supporting Information. For this purpose, we used 1-ethyl-3-(3-(dimethylamino)propyl)-carbodiimide (EDC)-*N*-hydroxy succinimide (NHS) mediated esterification process, as reported previously by us and others.[31−33] Once the reaction was finished, we separated the YFCD-conjugated magnetic nanoparticles using a magnet. The TEM image shown in Figure 2C shows the morphology of the YFCD-conjugated magnetic nanoparticle and indicates that the nanoparticle's size is ∼30 ± 6 nm. The size measurement by TEM matches very well with the DLS data, as reported in Table S1 in the Supporting Information. Energy-dispersive X-ray spectroscopy (EDX) mapping data from the nanoarchitecture, as reported in Figure S1A, and elemental mapping EDX data, as reported in Figure S1B, show the presence of Fe, C, O, and N, indicating that the YFCDs are conjugated with the magnetic nanoparticle. Figure 2D shows the FTIR spectrum of the YFCD-conjugated magnetic nanoparticle, where we can clearly see the presence of amide A, amide-I, amide-II, amide-III, and other bands. The presence of these bands indicates the coupling of the YFCDs with the magnetic nanoparticles via the esterification process.[31,32] Figure 2F shows the XPS data for the YFCD-conjugated magnetic nanoparticles, which clearly indicate the presence of a C 1s peak at 284.8 eV, an O 1s peak at 532.5 eV, a N 1s peak at 398.1 eV, and an Fe 2p peak at 712.4 eV.[31,32] We measured the superparamagnetic properties of the YFCD-attached magnetic nanoparticle using as SQUID magnetometer, and we obtained a specific saturation magnetization of ∼29.4 emu/g.

As shown in Figure 1D, in the fourth step we the conjugated anti-PD-L1 monoclonal antibody with the magnetic-nanoparticle-attached YFCDs. For this purpose, we used the EDC-NHS-mediated esterification process with the amine group of the antibody and the functionalized acid group of nanoarchitectures, as reported previously by us and others.[31,32,34] Once the reaction was finished, we separated the anti-PD-L1 monoclonal antibody-conjugated magnetic-nanoparticle-attached YFCDs using a magnet. To understand the amount of anti-PD-L1 monoclonal antibodies attached to the YFCDS-attached magnetic nanoparticles, we performed thermogravimetric analysis, as reported in Figure S1C in the Supporting Information. This analysis indicated that the weight percentage of the antibodies was around 4.1%. Figure 3E shows the emission spectrum from the nanoarchitecture at an excitation wavelength of 480 nm. By measuring the fluorescence intensity from the quinine sulfate standard and the anti-PD-L1 monoclonal antibody-conjugated magnetic-nanoparticle-attached YFCDs, we determined the PLQY of the nanoarchitecture to be 0.26 at an excitation wavelength of 480 nm. Figure 3F shows the time-dependent photo luminescence decay profiles of the anti-PD-L1 monoclonal antibody-conjugated magnetic-nanoparticle-attached YFCDs at an excitation wavelength of 480 nm. The observed time-resolved decays can be fit very well by a double-exponential function with τ_1 = 1.9 ns and τ_3 = 12.6 ns.

2.3. Finding the Photostability and Cytotoxicity of Antibody-Conjugated Magnetic-Nanoparticle-Attached YFCD Nanoarchitectures. Since photostability is one of the most important parameters for the optical imaging of biomolecules,[30−37] we determined the photostability of the anti-PD-L1 monoclonal antibody-conjugated magnetic-nanoparticle-attached YFCD-based nanoarchitectures. For this purpose, we performed time-dependent luminescence experiments for 2 h using an excitation wavelength of 480 nm. As reported in Figure 3G, the luminescence intensity from anti-PD-L1 monoclonal antibody-conjugated magnetic-nanoparticle-attached YFCD-based nanoarchitectures changed less than 5%, even after 2 h of exposure to 480 nm light. The data clearly show that the anti-PD-L1 monoclonal antibody-conjugated magnetic-nanoparticle-attached YFCD-based nanoarchitecture is photostable for bioimaging purposes. Since cytotoxicity is an important parameter for bioimaging applications,[30−37] we next determined the possible toxicity of the anti-PD-L1 monoclonal antibody-conjugated magnetic-nanoparticle-attached YFCD-based nanoarchitectures. For this purpose, we used breast cancer SK-BR-3 cells, normal skin HaCaT cells, prostate cancer LnCaP cells, and lung cancer H1264 and A549 cells.[20,31,32,34]

Initially, all cells were treated with the nanoarchitecture for 48 h. After that, we used an MTT (3-(4,5-dimethylthiazol-2-yl)-2,5-diphenyltetrazolium bromide) assay to determine the cell viability.[20,31,32,34] The experimental details for the cell viability assays are reported in the Supporting Information. As reported in Figure 4A, our experimental data show that the cell viability hardly changed after treatment with the magnetic-nanoparticle-attached YFCDs based nanoarchitectures, indicating that the nanoarchitectures are highly biocompatible.

2.4. Demonstrating That Antibody-Conjugated Nanoarchitectures Can Be Used for the Selective Separation and the Accurate Identification of PD-L1-Expressing Exosomes. Due to the good photoluminescence quantum yield, photostability, superparamagnetic property, and high biocompatibility of the anti-PD-L1 monoclonal antibody-conjugated magnetic-nanoparticle-attached YFCD-based nanoarchitectures, we explored the possibility of using the nanostructures to track PD-L1 (+) exosomes. For this purpose, we used human NSCLC H460 cells lines, which express a high amount of the PD-L1 (+) exosomes, A549 lung cancer cells lines, which express a low amount of the PD-L1 (+) exosomes, and the normal skin HaCaT cell line, which does not express PD-L1 (+) exosomes. All cells were cultured using an ATCC (American Type Culture Collection) culture medium until they reached 60−70% confluency.[19,20] The experimental details for the cell culture are reported in the Supporting Information. After that, we replaced the culture medium with the exosome-depleted medium.[19,20] Next, non-small-cell lung cancer H460 cells, A549 lung cancer cells, and normal skin HaCaT cells were cultured for another three days. At the end, PD-L1 (+) exosomes and other types of exosomes were separated by differential centrifugation by removing cell debris and other different types of vesicles, as reported previously by us and others.[19−24] After that, we used DLS and SEM techniques to find the size distribution of the exosomes separated from different cell lines, as reported in Figures S2 and S3 and Table S2 in the Supporting Information. Using the DLS data reported in Table S2 and SEM data for exosomes separated from H460 and HaCaT cell lines, we found that the size of exosomes varies between 100 and 160 nm. We have also used the human PD-L1 enzyme-linked immunoassay kit for the quantitation of the PD-L1 (+) exosomes.[13−17] The ELISA data, shown in Figure 4B, indicate that the percentage of PD-

https://doi.org/10.1021/acsomega.2c01210
ACS Omega 2022, 7, 16035−16042

L1 (+) exosomes is much higher for non-small-cell lung cancer H460 cells lines than for A549 lung cancer cells lines. We did not observe detectable PD-L1 (+) exosomes in case of the normal skin HaCaT cell line.

Next, to understand whether anti-PD-L1 monoclonal antibody-conjugated magnetic-nanoparticle-attached YFCD-based nanoarchitectures can be used for the accurate capture and selective identification of PD-L1 (+) exosomes, we mixed the nanoarchitectures (500 μg/mL) with cell culture supernatants. After being mixed continuously for 30 min, the nanoarchitecture-attached exosomes were separated using a bar magnet, as shown in Figure 4C. After that, we also used the human PD-L1 enzyme-linked immunoassay kit for the quantitation of the PD-L1 (+) exosomes.[13−17] The experimental ELISA results are very similar to those we obtained by differential centrifugation. After magnetic separation, using the ELISA data, we found that the percentage of PD-L1 (+) exosomes is around five-times higher for non-small-cell lung cancer H460 cells lines than for A549 lung cancer cells lines. Additionally, we did not observe detectable PD-L1 (+) exosomes for normal skin HaCaT cell line. To compare the magnetic separation and exosome imaging efficiency of the nanoarchitecture with those of the separate magnetic nanoparticles and YFCDs , we separately performed the PD-L1 (+) exosome separation experiment with lung cancer H460 cell culture supernatants using the anti-PDL1 monoclonal antibody-conjugated carbon dots (500 μg/mL) and the anti-PDL1 monoclonal antibody-conjugated iron oxide nanoparticles (500 μg/mL). We used the PD-L1 enzyme-linked immunoassay kit for the quantitation of the PD-L1 (+) exosomes. As reported in Table S3 in the Supporting Information, the observed separation of PD-L1 (+) exosomes is 0% for YFCDs and 98 ± 2% for both the anti-PDL1 monoclonal antibody-conjugated iron oxide nanoparticles and the anti-PDL1 monoclonal antibody-conjugated nanoarchitectures. Similarly, as reported in Figure S4A and B in the Supporting Information, we did not observe any fluorescence image from the separated PD-L1 (+) exosomes when they were separated by anti-PDL1 monoclonal antibody-conjugated iron oxide nanoparticles in the absence of YFCDs. Similarly the fluorescence image shown in Figure S4C in the Supporting Information, shows the absence of PD-L1 (+) exosomes after separation when we tried to separate them using antibody-attached YFCDs. All the above data clearly show that the conjugation of YFCDs with magnetic nanoparticles is necessary for the separation and imaging of PD-L1 (+) exosomes from the cell culture supernatant.

The TEM image shown in Figure 4D clearly indicates that the anti-PD-L1 monoclonal antibody-conjugated nanoarchitectures are attached on the surfaces of the PD-L1 (+) exosomes. Similarly, the yellow fluorescence image of the PD-L1 (+) exosomes shown in Figure 4F shows that the anti-PD-L1 monoclonal antibody-conjugated magnetic-nanoparticle-attached YFCD-based nanoarchitectures can identify PD-L1 (+) exosomes after magnetic separation. Our experimental data clearly indicate that the anti-PD-L1 monoclonal antibody-conjugated magnetic-nanoparticle-attached YFCD-based nanoarchitectures are capable of the accurate separation and identification of PD-L1 (+) exosomes via fluorescence imaging.

Next, to find out whether the anti-PD-L1 monoclonal antibody-conjugated magnetic-nanoparticle-attached YFCD-based nanoarchitectures have the capability for the selective tracking of PD-L1 (+) exosomes, we also performed the same experiment with A549 lung cancer cells lines, which express a low amount of PD-L1 (+) exosomes, and the normal skin HaCaT cell line, which expresses the PD-L1 (−) exosome. As shown in Figure 4G, the yellow fluorescence image of the PD-L1 (+) exosomes shows that the anti-PD-L1 monoclonal antibody-conjugated nanoarchitectures can identify very few PD-L1 (+) exosomes after magnetic separation, which clearly shows that the number of PD-L1 (+) exosomes expressed by A549 lung cancer cells lines is much lower compared to that expressed by the lung cancer H460 cells lines. Similarly, as shown in Figure 4H, no PD-L1 (+) exosomes were separated by the anti-PD-L1 monoclonal antibody-conjugated nanoarchitectures from the normal skin HaCaT cell line. The above data clearly show that anti-PD-L1 monoclonal antibody-conjugated nanoarchitecture-based separation and identification of PD-L1 (+) exosomes is highly selective. Our experimental results also indicate that the normal skin HaCaT cell line does not express detectable PD-L1 (+) exosomes.

To understand whether anti-PD-L1 monoclonal antibody-conjugated nanoarchitectures can be used for the selective capture and identification of PD-L1 (+) exosomes from blood samples, we have used exosome-infected citrated whole rabbit blood as a proof-of-concept of clinical setting applications. For this purpose, 12 000 exosomes/mL PD-L1 (+) exosomes were injected into 5 mL of whole blood. After that, we added one million peripheral blood mononuclear cells per milliliter into the blood sample. In next step, the mixture was shaken gently for 2 h. We then combined the mixture with the nanoarchitectures (500 μg/mL). After the mixture was mixed for half an hour, nanoarchitecture-attached exosomes were separated using a bar magnet. Using the human PD-L1 enzyme-linked immunoassay kit, we found a PD-L1 (+) exosomes recovery of about 100%, as reported in Figure S5 in the Supporting Information. Figure 4I shows the yellow fluorescence image of the PD-L1 (+) exosomes after magnetic separation from whole blood. All the above data clearly indicate that the anti-PD-L1 monoclonal antibody-conjugated magnetic-nanoparticle-attached YFCD-based nanoarchitectures are capable of the accurate separation and identification of PD-L1 (+) exosomes via fluorescence imaging from an infected blood sample.

3. CONCLUSIONS

In summary, we have designed and synthesized bioconjugated magnetic-nanoparticle-attached YFCD-based nanoarchitectures for the magnetic separation and identification of PD-L1 (+) exosomes. More importantly, using different microscopic and spectroscopic characterization techniques, we have demonstrated that the bioconjugated magnetic-nanoparticle-attached YFCD-based nanoarchitectures exhibit a good photoluminescence quantum yield (23%) and superparamagnetic (28.6 emu/g) behavior. Additionally, they are photostable and highly biocompatible. In this work, our finding reveals that anti-PD-L1 monoclonal antibody-conjugated magnetic-nanoparticle-attached YFCD-based nanoarchitectures are capable of accurately separating and tracking PD-L1 (+) exosomes from cancer cell lines as well as from a blood sample. In addition, using two different human lung cancer cells lines that expressed high and low amounts of PD-L1 (+) exosomes, we showed that the nanoarchitectures are capable of the effective separation and accurate identification of PD-L1 (+) exosomes via yellow luminescence imaging. On the other hand, using a cell line that expressed the PD-L1 (−) exosome,

https://doi.org/10.1021/acsomega.2c01210
ACS Omega 2022, 7, 16035−16042

we further demonstrated that the nanoarchitecture-based separation and tracking of PD-L1 (+) exosomes is highly selective. As a proof-of-concept of clinical setting applications, we used a PD-L1 (+) exosome-infected whole-blood sample to demonstrate that nanoarchitectures are capable of separating and imaging PD-L1 (+) exosomes from infected blood sample. Taken together, reported data show the design of an innovative nanoplatform that has the potential to be a powerful tool for improving lung cancer detection and therapy.

■ ASSOCIATED CONTENT

Supporting Information

The Supporting Information is available free of charge at https://pubs.acs.org/doi/10.1021/acsomega.2c01210.

Design and characterization of the anti-PD-L1 monoclonal antibody=conjugated magnetic-nanoparticle-attached YFCD-based nanoarchitectures and other experiments, including cell cultures, separation of the PD-L1 (+) exosomes, and luminescence imaging (PDF)

■ AUTHOR INFORMATION

Corresponding Author

Paresh Chandra Ray − *Department of Chemistry and Biochemistry, Jackson State University, Jackson, Mississippi 39217, United States;* orcid.org/0000-0001-5398-9930; Email: paresh.c.ray@jsums.edu; Fax: +16019793674

Authors

Avijit Pramanik − *Department of Chemistry and Biochemistry, Jackson State University, Jackson, Mississippi 39217, United States;* orcid.org/0000-0002-4623-2099

Shamily Patibandla − *Department of Chemistry and Biochemistry, Jackson State University, Jackson, Mississippi 39217, United States*

Ye Gao − *Department of Chemistry and Biochemistry, Jackson State University, Jackson, Mississippi 39217, United States*

Lauren R. Corby − *Department of Chemistry and Biochemistry, Jackson State University, Jackson, Mississippi 39217, United States*

Md Mhahabubur Rhaman − *Department of Chemistry and Biochemistry, Jackson State University, Jackson, Mississippi 39217, United States*

Sudarson Sekhar Sinha − *Department of Chemistry and Biochemistry, Jackson State University, Jackson, Mississippi 39217, United States;* orcid.org/0000-0002-0831-2338

Complete contact information is available at: https://pubs.acs.org/10.1021/acsomega.2c01210

Notes

The authors declare no competing financial interest.

■ ACKNOWLEDGMENTS

Dr. Ray thanks NSF-PREM (Grant DMR-1826886) for their generous funding, which was used for the design of the nanoarchitectures. We are also thankful for NIH-NIMHD Grant U54MD015929-01 for lung cancer research and the bioimaging core facility.

■ REFERENCES

(1) The American Cancer Society medical and editorial content team. *Key Statistics for Lung Cancer*. 2022. https://www.cancer.org/cancer/lung-cancer/about/key-statistics.html (accessed 2022-01-24).

(2) World Health Organization. *Cancer*. 2022. https://www.who.int/news-room/fact-sheets/detail/cancer (accessed 2022-01-24)

(3) Siegel, R. L.; Miller, K. D.; Fuchs, H. E.; Jemal, A. Cancer Statistics. *J. Clin.* **2021**, *71*, 7−33.

(4) Pantel, K.; Alix-Panabières, C. Liquid Biopsy and Minimal Residual Disease - Latest Advances and Implications for Cure. *Nat. Rev. Clin. Oncol.* **2019**, *16*, 409−424.

(5) Finck, A.; Gill, S. I.; June, C. H. Cancer Immunotherapy Comes of Age and Looks for Maturity. *Nat. Commun.* **2020**, *11*, 3325.

(6) Lim, S. M.; Hong, M. H.; Kim, H. R. Immunotherapy for Non-Small Cell Lung Cancer: Current Landscape and Future Perspectives. *Immune Netw.* **2020**, *20* (1), No. e10.

(7) Sheridan, C. Exosome Cancer Diagnostic Reaches Market. *Nat. Biotechnol.* **2016**, *34*, 359−360.

(8) Wang, G.; Xie, L.; Li, B.; Sang, W.; Yan, J.; Li, J.; Tian, H.; Li, W.; Zhang, Z.; Tian, Y.; Dai, Y. A nanounit strategy reverses immune suppression of exosomal PDL-1 and is associated with enhanced ferroptosis. *Nat. Commum.* **2021**, *12*, 5733.

(9) Daassi, D.; Mahoney, K. M.; Freeman, G. J. The Importance of Exosomal PDL1 in Tumour Immune Evasion. *Nat. Rev. Immunol.* **2020**, *20*, 209−215.

(10) Chen, G.; Huang, A. C.; Zhang, W.; Zhang, G.; Wu, M.; Xu, W.; Yu, Z.; Yang, J.; Wang, B.; Sun, H.; Xia, H.; Man, Q.; Zhong, W.; Antelo, L. F.; Wu, B.; Xiong, X.; Liu, X.; Guan, L.; Li, T.; Liu, S.; Yang, R.; Lu, Y.; Dong, L.; McGettigan, S.; Somasundaram, R.; Radhakrishnan, R.; Mills, G.; Lu, Y.; Kim, J.; Chen, Y. H.; Dong, H.; Zhao, Y.; Karakousis, G. C.; Mitchell, T. C.; Schuchter, L. M.; Herlyn, M.; Wherry, E. J.; Xu, X.; Guo, W. Exosomal PD-L1 Contributes to Immunosuppression and is Associated with anti-PD-1 Response. *Nature* **2018**, *560*, 382−386.

(11) Poggio, M.; Hu, T.; Pai, C. C.; Chu, B.; Belair, C. D.; Chang, A.; Montabana, E.; Lang, U. E.; Fu, Q.; Fong, L.; Blelloch, R. Suppression of Exosomal PD-L1 Induces Systemic Anti-Tumor Immunity and Memory. *Cell* **2019**, *177*, 414−427.

(12) Huang, M.; Yang, J.; Wang, T.; Song, J.; Xia, J.; Wu, L.; Wang, W.; Wu, Q.; Zhu, Z.; Song, Y.; Yang, C. Homogeneous, Low-volume, Efficient, and Sensitive Quantitation of Circulating Exosomal PD-L1 for Cancer Diagnosis and Immunotherapy Response Prediction. *Angew. Chem.* **2020**, *132*, 4830−4835.

(13) Gordon, S. R.; Maute, R. L.; Dulken, B. W.; Hutter, G.; George, B. M.; McCracken, M. N.; Gupta, R.; Tsai, J. M.; Sinha, R.; Corey, D.; Ring, A. M.; Connolly, A. J.; Weissman, I. L. PD-1 Expression by Tumour-Associated Macrophages Inhibits Phagocytosis and Tumour Immunity. *Nature* **2017**, *545*, 495−499.

(14) Wang, X.; Shang, H.; Ma, C.; Chen, L. A Fluorescence Assay for Exosome Detection Based on Bivalent Cholesterol Anchor Triggered Target Conversion and Enzyme-Free Signal Amplification. *Anal. Chem.* **2021**, *93*, 8493−8500.

(15) Li, B.; Pan, W.; Liu, C.; Guo, J.; Shen, J.; Feng, J.; Luo, T.; Situ, B.; Zhang, Y.; An, T.; Xu, C.; Zheng, W.; Zheng, L. Homogenous Magneto-Fluorescent Nanosensor for Tumor-Derived Exosome Isolation and Analysis. *ACS Sens.* **2020**, *5*, 2052−2060.

(16) Vinduska, V.; Gallops, C. E.; O'Connor, R.; Wang, Y.; Huang, X. Exosomal Surface Protein Detection with Quantum Dots and Immunomagnetic Capture for Cancer Detection. *Nanomaterials* **2021**, *11*, 1853.

(17) Wang, C.; Huang, C. H.; Gao, Z.; Shen, J.; He, J.; MacLachlan, A.; Ma, C.; Chang, Y.; Yang, W.; Cai, Y.; Lou, Y.; Dai, S.; Chen, W.; Li, F.; Chen, P. Nanoplasmonic Sandwich Immunoassay for Tumor-Derived Exosome Detection and Exosomal PD-L1 Profiling. *ACS Sensors* **2021**, *6* (9), 3308−3319.

(18) Kwizera, E. A.; O'Connor, R.; Vinduska, V.; Williams, M.; Butch, E. R.; Snyder, S. E.; Chen, X.; Huang, X. Molecular Detection and Analysis of Exosomes Using Surface-Enhanced Raman Scattering Gold Nanorods and a Miniaturized Device. *Theranostics* **2018**, *8*, 2722−2738.

(19) Pramanik, A.; Mayer, J.; Patibandla, S.; Gates, K.; Gao, Ye; Davis, D.; Seshadri, R.; Ray, P. C. Mixed-Dimensional Hetero-

structure Material-Based SERS for Trace Level Identification of Breast Cancer-Derived Exosomes. *ACS-Omega* **2020**, *5* (27), 16602−16611.
(20) Pramanik, A.; Gates, K.; Patibandla, S.; Davis, D.; Begum, S.; Iftekhar, R.; Alamgir, S.; Paige, S.; Porter, M. M.; Ray, P. C. Water-Soluble and Bright Luminescent Cesium-Lead-Bromide Perovskite Quantum Dot-Polymer Composites for Tumor-Derived Exosome Imaging. *ACS Appl. Bio Mater.* **2019**, *2*, 5872−5879.
(21) Yan, H.; Li, Y.; Cheng, S.; Zeng, Y. Advances in Analytical Technologies for Extracellular Vesicles. *Anal. Chem.* **2021**, *93*, 4739−4774.
(22) Kalluri, R.; LeBleu, V. S. The Biology, Function, and Biomedical Applications of Exosomes. *Science* **2020**, *367*, No. eaau6977.
(23) Qin, Y.; Bai, Y.; Huang, P.; Wu, F. Y. Dual-Emission Carbon Dots for Ratiometric Fluorescent Water Sensing, Relative Humidity Sensing, and Anticounterfeiting Applications. *ACS Applied Nano Materials* **2021**, *4* (10), 10674−10681.
(24) Anwar, S.; Ding, H.; Xu, M.; Hu, X.; Li, Z.; Wang, J.; Liu, L.; Jiang, L.; Wang, D.; Dong, C.; Yan, M.; Wang, Q.; Bi, H. Recent Advances in Synthesis, Optical Properties, and Biomedical Applications of Carbon Dots. *ACS Appl. Energy Mater.* **2019**, *2*, 2317−2338.
(25) Wareing, T. C.; Gentile, P.; Phan, A. N. Biomass-based carbon dots: current development and future perspectives. *ACS Nano* **2021**, *15*, 15471−15501.
(26) Yang, Y.; Kannisto, E.; Patnaik, S. K.; Reid, M. E.; Li, L.; Wu, Y. Ultrafast Detection of Exosomal RNAs via Cationic Lipoplex Nanoparticles in a Micromixer Biochip for Cancer Diagnosis. *ACS Appl. Nano Mater.* **2021**, *4*, 2806−2819.
(27) Wareing, T. C.; Gentile, P.; Phan, A. N. Biomass-based carbon dots: current development and future perspectives. *ACS Nano* **2021**, *15*, 15471−15501.
(28) Xu, D.; Lin, Q.; Chang, H.-T. Recent Advances and Sensing Applications of Carbon Dots. *Small Methods* **2020**, *4*, 1900387.
(29) Zhu, Z.; Liu, C.; Song, X.-M.; Mao, Q.; Ma, T. Carbon Dots as an Indicator of Acid−Base Titration and a Fluorescent Probe for Endoplasm Reticulum Imaging. *ACS Appl. Bio Mater.* **2021**, *4*, 3623−3629.
(30) Lu, W.; Jiao, Y.; Gao, Y.; Qiao, J.; Mozneb, M.; Shuang, S.; Dong, C.; Li, C.-Z. Bright Yellow Fluorescent Carbon Dots as a Multifunctional Sensing Platform for the Label-Free Detection of Fluoroquinolones and Histidine. *ACS Appl. Mater. Interfaces* **2018**, *10*, 42915−42924.
(31) Pramanik, A.; Jones, S.; Pedraza, F.; Vangara, A.; Sweet, C.; Williams, M. S.; Ruppa-Kasani, V.; Risher, S. E.; Sardar, D.; Ray, P. C. Fluorescent, Magnetic Multifunctional Carbon Dots for Selective Separation, Identification, and Eradication of Drug-Resistant Superbugs. *ACS Omega* **2017**, *2*, 554−562.
(32) Pramanik, A.; Vangara, A.; Nellore, B. P. V.; Sinha, S. S.; Chavva, S. R.; Jones, S.; Ray, P. C. Development of Multifunctional Fluorescent-Magnetic Nanoprobes for Selective Capturing and Multicolor Imaging of Heterogeneous Circulating Tumor Cells. *ACS Appl. Mater. Interfaces* **2016**, *8*, 15076−15085.
(33) Pramanik, A.; Begum, S.; Rightsell, C.; Gates, K.; Zhang, Q.; Jones, S.; Gao, Y.; Ruppa-Kasani, V.; Banerjee, R.; Shukla, J.; Ignatius, A.; Sardar, D.; Han, F. X.; Ray, P. C. Designing Highly Crystalline Multifunctional Multicolor Luminescence Nanosystem for Tracking Breast Cancer Heterogeneity. *Nanoscale Adv.* **2019**, *1*, 1021−1034.
(34) Pramanik, A.; Patibandla, S.; Gao, Y.; Gates, K.; Ray, P. C. Water Triggered Synthesis of Highly Stable and Biocompatible 1D Nanowire, 2D Nanoplatelet, and 3D Nanocube CsPbBr3 Perovskites for Multicolor Two-Photon Cell Imaging. *J. Am. Chem. Soc. Au* **2021**, *1* (1), 53−65.
(35) Wang, J.; Li, Q.; Zheng, J.; Yang, Y.; Liu, X.; Xu, B. N, B-codoping induces high-efficiency solid-state fluorescence and dual emission of yellow/orange carbon dots. *ACS Sustainable Chem. Eng.* **2021**, *9*, 2224−2236.
(36) Meng, T.; Wang, Z.; Yuan, T.; Li, X.; Li, Y.; Zhang, Y.; Fan, L. Gram-scale synthesis of highly efficient rare-earth element-free red/green/blue solid-state bandgap fluorescent carbon quantum rings for white light-emitting diodes. *Angew. Chem., Int. Ed.* **2021**, *60*, 16343−16348.
(37) Liang, T.; Liu, E.; Li, M.; Ushakova, E. V.; Kershaw, S. V.; Rogach, A. L.; Tang, Z.; Qu, S. Morphology control of luminescent carbon nanomaterials: from dots to rolls and belts. *ACS Nano* **2021**, *15*, 1579−1586.

https://doi.org/10.1021/acsomega.2c01210
ACS Omega 2022, 7, 16035−16042